



## Rational design of defect metal oxide/covalent organic frameworks Z-scheme heterojunction for photoreduction CO<sub>2</sub> to CO

Yan Wang <sup>a,b</sup>, Zhao Hu <sup>c</sup>, Wei Wang <sup>a</sup>, Yanan Li <sup>a</sup>, Haichuan He <sup>a</sup>, Liu Deng <sup>a,b,\*</sup>, Yi Zhang <sup>a</sup>, Jianhan Huang <sup>a</sup>, Ning Zhao <sup>b</sup>, Guipeng Yu <sup>a</sup>, You-Nian Liu <sup>a,d,\*</sup>

<sup>a</sup> Hunan Provincial Key Laboratory of Micro & Nano Materials Interface Science, College of Chemistry and Chemical Engineering, Central South University, Changsha, Hunan 410083, PR China

<sup>b</sup> State Key Laboratory of Coal Conversion, Institute of Coal Chemistry, CAS, Taiyuan, Shanxi 030001, PR China

<sup>c</sup> State Key Laboratory Breeding Base of Green Pesticide & Agricultural Bioengineering, Key Laboratory of Green Pesticide & Agricultural Bioengineering of Ministry of Education, State-Local Joint Laboratory for Comprehensive Utilization of Biomass Center for R&D of Fine Chemicals, Guizhou University, Guiyang, Guizhou 550025, PR China

<sup>d</sup> College of Material, Chemistry and Chemical Engineering, Hangzhou Normal University, Hangzhou, Zhejiang 311121, PR China



### ARTICLE INFO

#### Keywords:

Heterostructure  
Covalent organic frameworks  
CO<sub>2</sub> photoreduction  
Z-scheme  
Defect metal oxide

### ABSTRACT

Z-scheme heterostructure consisting of covalent organic frameworks (COF) and inorganic semiconductor possesses tremendous potential for achieving efficient photoreduction of CO<sub>2</sub>. However, the precise design and rationalization of the interaction between COF and inorganic semiconductors remains a great challenge. Herein, the interaction of different N-sites on T-COF framework with defect TiO<sub>2</sub> and stoichiometric TiO<sub>2</sub> is investigated by density functional theory. The theoretical analysis suggests that the amine group of T-COF could provide an energetically favored binding site towards defect TiO<sub>2</sub>. Accordingly, a stable Z-scheme heterostructure with well-defined chemical bonding between Ti<sup>3+</sup> and -NH<sub>2</sub>, and well-engineered geometry configuration through *in situ* anchoring defect TiO<sub>2</sub> on the surface of amine-functionalized T-COF sphere is designed. The obtained heterostructure exhibits a high CO<sub>2</sub>-to-CO conversion efficiency, with nearly 100 % CO selectivity and an apparent quantum efficiency of 6.81 % at 365 nm. This work could provide guidance for the rational design of Z-scheme heterostructure photocatalysts for photocatalytic applications in high efficiency.

### 1. Introduction

The energy conversion strategies, such as carbon dioxide conversion, water splitting and nitrogen reduction, offer promising routes for building a sustainable and environment friendly energy cycle [1–3]. In these strategies, covalent organic frameworks (COF), including porphyrin-based COF, bipyridine-based COF and triazine-based COF are commonly utilized as a state-of-the art photocatalyst for the CO<sub>2</sub> reduction, hydrogen evolution reaction and nitrogen reduction [4–10]. However, it is difficult for a single COFs to serve as photocatalyst to simultaneously satisfy all the requirements for industrial photocatalytic efficiency, such as strong redox ability, high charge separation efficiency, wide light absorption range and long-term stability. Instead of developing novel framework construction, coupling with other semiconductor to form heterojunction is an alternative strategy to enhance

the performance of COF catalysts [11–13]. For instance, heterojunction composites fabricated from COF and other inorganic semiconductors, such as  $\alpha$ -Fe<sub>2</sub>O<sub>3</sub>, Bi<sub>2</sub>WO<sub>6</sub>, TiO<sub>2</sub>, etc., have been intensively investigated, and they exhibited an enhanced performance over those only have a single phase structure [14–17]. Nevertheless, these kinds of COF-based photocatalysts still fail to meet the strict criteria including high selectivity and stability, mainly due to mismatched band structure for the specific product, undefined transmission channel for the charge delivery and weak interaction between them.

Recently, the electronic structure modulation is generally utilized to optimize energy band structure in the photocatalyst and achieve the better conversion efficiency, which have emerged as a research frontier in photocatalysis [18–20]. The defect engineering has been widely considered as promising approaches to modulate the electronic structure of metal oxide [21–23]. Compared to the stoichiometric metal oxide, the

\* Corresponding authors at: Hunan Provincial Key Laboratory of Micro & Nano Materials Interface Science, College of Chemistry and Chemical Engineering, Central South University, Changsha, Hunan 410083, PR China

E-mail addresses: [dengliu@csu.edu.cn](mailto:dengliu@csu.edu.cn) (L. Deng), [liuyounian@csu.edu.cn](mailto:liuyounian@csu.edu.cn) (Y.-N. Liu).

defective metal oxides exhibit improved the photogenerated charge-carriers transfer and separation efficiency [24,25]. In addition, it is important to build the well-defined electron transmission channel between the two components to achieve a rational design of optimal heterojunction photocatalysts [26–28]. Most recently, several interfaces connection models, such as van der Waals forces, electrostatic interaction, hydrogen bonding and chemical bonding, have been reported to correlate the existence of chemical bonding with the performance of photocatalyst, such as the tight and stable interface [29,30]. Therefore, it is imperative to design a Z-scheme system with the following characteristics. (i) well-defined structure with both components being exposed to reactive substrates and light irradiation; (ii) suitable defect introduction for the proper band structure; and (iii) specific chemical bond connection between the two composites for the fast migration and separation of electrons and holes. The coordinatively unsaturated metal centers for the metal oxide on the COF surface are good choice to address the above issues, which provides the defined structures for further investigation on the reaction mechanism. However, no practical strategies for effectively coupled the COF and deficient metal oxide semiconductor with specific metal–N covalent connection has been reported yet.

Herein, we present a theoretical-guided strategy of COF/defect-TiO<sub>2</sub> heterojunction photocatalyst for the selective reduction of CO<sub>2</sub> to CO. The adsorption energy using density functional theory (DFT) calculation suggests that the intrinsic deficient TiO<sub>2</sub> can be formed on the surface of NH<sub>2</sub>–T–COF through Ti–N covalent bonding, where Ti<sup>3+</sup>–N on amino group is suggested to be the most active sites. Then, a stable Z-scheme system with well-engineered geometry configuration and intimately contacted heterointerface through anchoring defect TiO<sub>2</sub> on the surface of amine-functionalized COF sphere, is prepared. The Ti–N bonding between d-TiO<sub>2</sub> and NH<sub>2</sub>–T–COF not only results in a well-combined interface, but acts as a good electrons delivery channel between them, forming a direct Z-scheme heterostructure. The obtained NCTS-2 heterostructure exhibits an excellent activity for photocatalytic CO<sub>2</sub> reduction, giving a 7.51 μmol of CO in a 4 h reaction with a nearly 100 % CO selectivity and an apparent quantum efficiency of 6.81 % at 365 nm, much higher than that of pure d-TiO<sub>2</sub>. *In situ* DRIFTS results suggest that the significantly enhanced catalytic activity and selectivity are ascribed to the synergistic effect of Ti sites and rich-N groups of NH<sub>2</sub>–T–COF framework, in which the rich-N groups not only serve as a host for CO<sub>2</sub> molecules and Ti sites, but also facilitate the activation of CO<sub>2</sub> molecules and inhibit the competitive H<sub>2</sub> evolution. This work highlights that building the Z-scheme COF system with specific bonding between the components not only provide a tight and stable interface as well as a definite electrons delivery channel, but also regulate active sites, which jointly improve CO<sub>2</sub>RR performance in the CO production.

## 2. Experimental section

### 2.1. Materials

2,4,6-Tris(4-aminophenyl)-1,3,5-triazine and 1,3,5-benzene tricarboxaldehyde were purchased from Yanshen Technology (Jilin, Changchun, China). Tetrabutyl titanate (TBT) was brought from Sino-pharm (Shanghai, China). CO<sub>2</sub> (99.99 %) were purchased from Saizhong Gas (Changsha, China). All other solvents and reagents were obtained from commercial sources and used without further purification unless otherwise noted.

### 2.2. Synthesis of NH<sub>2</sub>–T–COF

NH<sub>2</sub>–T–COF was prepared according to the procedures of T–COF. [16] Here, excessive 4,6-tris(4-aminophenyl)-1,3,5-triazine (0.05 mmol, 17.2 mg) and 1,3,5-benzenetricarboxaldehyde (0.04 mmol, 6.5 mg) were used as monomers to construct NH<sub>2</sub>–TCOF. The reaction conditions were the same as for T–COF.

### 2.3. Synthesis of d-TiO<sub>2</sub>

The d-TiO<sub>2</sub> was synthesized by modified literature procedures [31]. 0.5 mL of TBT was added to 15 mL of ethanol followed by vigorous stirring for 30 min. Then, 50 μL of hydrofluoric acid (40 %) and 1.5 mL of deionized water were added dropwise to the reaction system, respectively. Then stirring for another 30 min, the resulting solution was transferred into Teflon-lined autoclave (50 mL) and subsequently kept at 120 °C for 24 h. After the reaction was cooled to room temperature, the precipitate was collected, washed with ethanol, then dried under vacuum at 60 °C for 8 h.

### 2.4. Synthesis of NCTS

NH<sub>2</sub>–T–COF (40 mg) was fully dispersed in the ethanol solvent (15 mL). Then, a certain amount of TBT was added to the solution following vigorous stirring for 30 min. After that, 10 μL of hydrofluoric acid (40 %) and 300 μL of deionized water were added dropwise to the reaction system, respectively. Then stirring for another 30 min, the resulting solution was transferred into Teflon-lined autoclave (50 mL) and subsequently kept at 120 °C for 24 h. After the reaction was cooled to room temperature, the precipitate was collected, washed with ethanol, then dried under vacuum at 60 °C for 8 h. By varying the amount of the precursor TBT (40, 65, 90 μL), NCTS-X with different d-TiO<sub>2</sub> content were obtained (X = 1, 2, 3).

### 2.5. Photocatalytic CO<sub>2</sub> reduction reaction

The photocatalytic CO<sub>2</sub> reduction reaction was performed in a closed gas circulation system (Labsolar 6A, Beijing PerfectLight) under full solar-spectrum irradiation. Typically, the as-prepared photocatalyst (10 mg) was dispersed in a mixed solution of 50 mL acetonitrile and 30 mL ascorbic acid aqueous (0.1 M). Then, the obtained suspension solution was transferred to a Quartz and Pyrex glass hybrid reaction cell. After completing the evacuation of the air, ~80 kPa of pure CO<sub>2</sub> gas was injected into the airtight system. After adsorption equilibrium (~30 min), a 300 W Xe lamp (PLS-SXE300, PerfectLight, Beijing, China) was used at the top of the reactor as the light source, and cooling water was employed to control the temperature of the reaction system at 5 °C. The produced CO and H<sub>2</sub> was analyzed by gas chromatography (7890B, Agilent, CA, USA).

## 3. Results and discussion

### 3.1. Theoretical analysis

The interaction of different N-sites on T–COF framework[16] with defect TiO<sub>2</sub> and stoichiometric TiO<sub>2</sub> by density functional theory (DFT) calculations was investigated. As shown in Fig. S1, the rich-N groups on the T–COF skeleton are divided into three basic kinds: triazine ( $\sigma$ -N<sub>sp2</sub>), imine ( $\sigma$ -N<sub>sp2</sub>) and amine ( $\sigma$ -N<sub>sp3</sub>) groups. As presented in Fig. 1a–1c, the adsorption energy ( $E_{ads}$ ) between defect TiO<sub>2</sub> and N-sites of triazine, amine and imine groups are –0.68, –1.32, –1.90 eV, respectively, suggesting that amine groups possess more stronger interaction for defect TiO<sub>2</sub>. This proves that d-TiO<sub>2</sub> binding is more energetically favored to amine groups than to triazine and imine groups during the process of d-TiO<sub>2</sub> growing on the T–COF framework. More significantly, the DFT calculations suggest that the  $E_{ads}$  of amine groups on T–COF framework toward defect TiO<sub>2</sub> (–1.90 eV) is much larger than that of defect-free TiO<sub>2</sub> (–0.52 eV), indicating that defect TiO<sub>2</sub> is more energetically favored to rivet on the T–COF framework (Fig. 1d). These findings manifest that amine group could provide a more favored energetically binding site towards defect TiO<sub>2</sub> formation on the surface of T–COF than the imine and triazine group, resulting in a more efficient defect TiO<sub>2</sub> loading, as well as a much tighter and more stable interface. Therefore, the incorporation of more amine group within T–COF

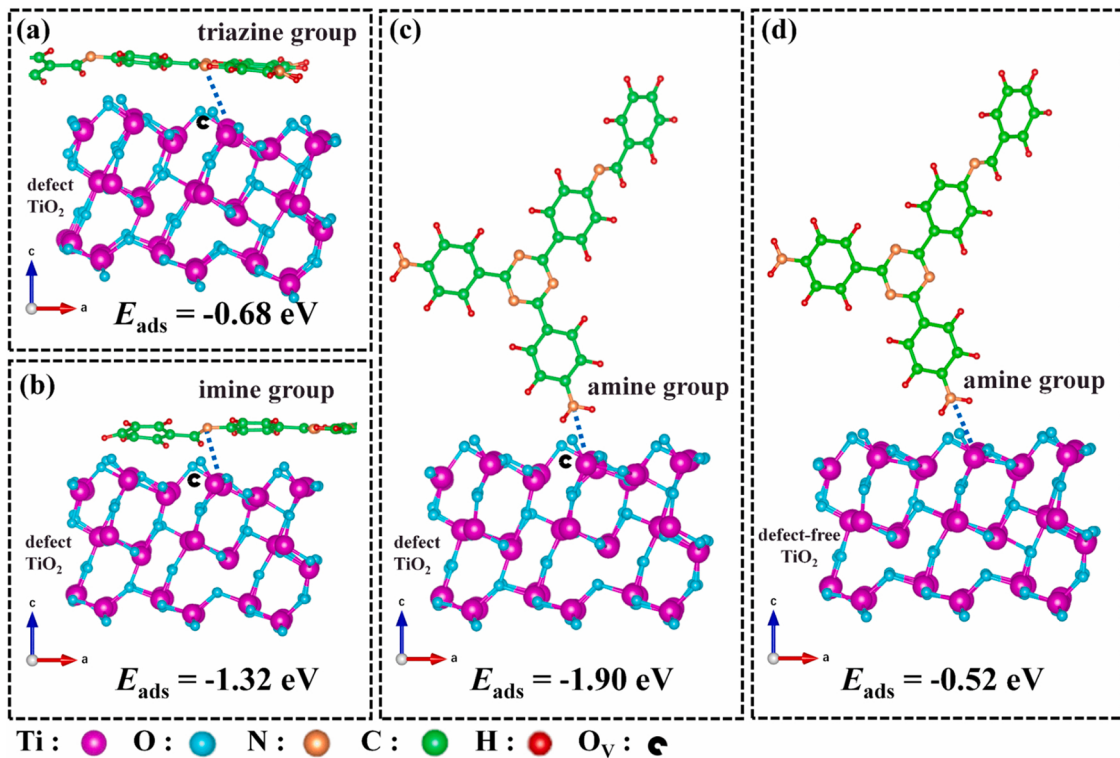


**Fig. 1.** Optimized structure model of different N-sites on T-COF framework adsorbed on the surface of defect  $\text{TiO}_2$  and defect-free  $\text{TiO}_2$ .  $E_{\text{ads}}$  is the adsorption energy.

skeleton is an effective strategy to stabilize bonded defect  $\text{TiO}_2$  for ultimate catalytic applications.

### 3.2. Synthesis and characterization of photocatalyst

Accordingly, we designed and fabricated surface-loaded defect  $\text{TiO}_2$  ( $\text{D-TiO}_2$ ) amine-functionalized T-COF ( $\text{NH}_2\text{-T-COF}$ ). The preparation processes of  $\text{NH}_2\text{-T-COF/D-TiO}_2$  spheres (NCTS) are illustrated in Fig. 2a. To ensure that the surface of the COF spheres loading more amine groups for  $\text{TiO}_2$  binding,[32] amine-functionalized T-COF was synthesized by the condensation of 1,3,5-benzenetricarboxaldehyde and an excess of (2,4,6-tris(4-aminophenyl)-1,3,5-triazine (see the details in Supporting information). As shown in Fig. S2, the zeta potential of  $\text{NH}_2\text{-T-COF}$  is significantly lower than that of T-COF, indicating an increase in the number of amine groups on the surface of  $\text{NH}_2\text{-T-COF}$ . The elemental analysis also shows that the N and H elements on the skeleton of  $\text{NH}_2\text{-T-COF}$  are higher than those of T-COF (Table S1). These results demonstrate that the amine groups are successfully decorated on the surface of T-COF sphere. In the Fourier transform infrared (FT-IR) spectra of  $\text{NH}_2\text{-T-COF}$  (Fig. S3), the peak at  $1686 \text{ cm}^{-1}$  attributed to the  $\text{C=O}$  stretching disappears, manifesting a high degree of polymerization. The crystallinity of  $\text{NH}_2\text{-T-COF}$  was confirmed by powder X-ray diffraction (PXRD). All peaks match well with those of the simulated AA stacking mode. And the peak at  $5.65^\circ$  shows a high intensity, indicating the successful preparation of  $\text{NH}_2\text{-T-COF}$  with high crystallinity (Fig. S4) [33]. Then, different masses of tetrabutyl titanate (TBT) as the precursor are uniformly dispersed on the surface of  $\text{NH}_2\text{-T-COF}$  sphere, following by one-step solvothermal reaction to obtain the defect  $\text{TiO}_2$ -decorated  $\text{NH}_2\text{-T-COF}$  spheres composites (NCTS). Thermogravimetric analysis (TGA) shows their excellent thermostability without obvious mass loss after heating up to  $200^\circ\text{C}$  under  $\text{N}_2$  atmosphere (Fig. S5).

The morphology of the samples was recorded by transmission electron microscopy (TEM) and scanning electron microscopy (SEM). As illustrated in Fig. 2b and S6, after *in situ* modification of  $\text{D-TiO}_2$  on

$\text{NH}_2\text{-T-COF}$ , the as-obtained NCTS still maintains the spherical morphology of  $\text{NH}_2\text{-T-COF}$ , and  $\text{D-TiO}_2$  nanoparticles can be clearly seen uniformly embedded on the surface of  $\text{NH}_2\text{-T-COF}$  spheres (Fig. 2c). The high-resolution TEM (HRTEM) image clearly shows the lattice fringes with an interplanar spacing of  $0.352 \text{ nm}$ , which is attributed to the (101) plane of anatase  $\text{TiO}_2$  (Fig. 2d) [34]. Moreover, the high-angle annular dark field TEM (HAADF-TEM) image and energy-dispersive X-ray spectroscopy (EDX) elemental mapping of NCTS-2 further prove that Ti element are evenly distributed within the framework of  $\text{NH}_2\text{-T-COF}$  sphere (Fig. 2e-h). It should be noted that the pure  $\text{D-TiO}_2$  prepared by the same solvothermal method exhibits an agglomerated state (Fig. S7). After introduction of  $\text{NH}_2\text{-T-COF}$ , the  $\text{D-TiO}_2$  nanoparticles can be uniformly dispersed on the surface of  $\text{NH}_2\text{-T-COF}$  sphere. These results manifest that the  $\text{NH}_2\text{-T-COF}$  framework can serve as the template to well anchor and stabilize  $\text{D-TiO}_2$  by the strong interaction.

The PXRD pattern of NCTS composites are shown in Fig. 3a. The diffraction peaks at  $5.65$ ,  $9.75$ ,  $11.25$  and  $14.95^\circ$  correspond to the (100), (110), (200) and (210) facets of  $\text{NH}_2\text{-T-COF}$  respectively, in agreement with the XRD pattern of simulated AA stacking mode,[33] and the peaks at  $25.28$ ,  $37.82$ ,  $48.05$ ,  $53.89$  and  $55.06^\circ$  attribute to the (101), (004), (200), (105) and (211) facets of  $\text{D-TiO}_2$ , respectively (Fig. S8), matching up with the simulated PXRD patterns of the typical anatase  $\text{TiO}_2$  (JCPDS No. 21-1272), which reveals that the crystal structure of the  $\text{NH}_2\text{-T-COF}$  and  $\text{D-TiO}_2$  are basically unchanged after the formation of the heterostructure composite. The FT-IR spectra of NCTS-2,  $\text{NH}_2\text{-T-COF}$  and  $\text{D-TiO}_2$  are shown in Fig. 3b. For pure  $\text{D-TiO}_2$ , the main peaks appearing at  $400\text{--}700 \text{ cm}^{-1}$  are attributed to  $\text{Ti-O}$  stretching and another two broad peaks at about  $3300\text{--}3500$  and  $1600\text{--}1650 \text{ cm}^{-1}$  correspond to the surface-adsorbed water and hydroxyl groups, respectively. These characteristic peaks all appear in the FT-IR spectra of NCTS-2, further suggesting the successful preparation of NCTS-2 heterostructure composite. As shown in Fig. S9, the newly formed  $\text{C=N}$  after polycondensation can be clearly observed in the solid-state  $^{13}\text{C}$  cross polarization magic angle spinning ( $^{13}\text{C}$  CP-MAS)

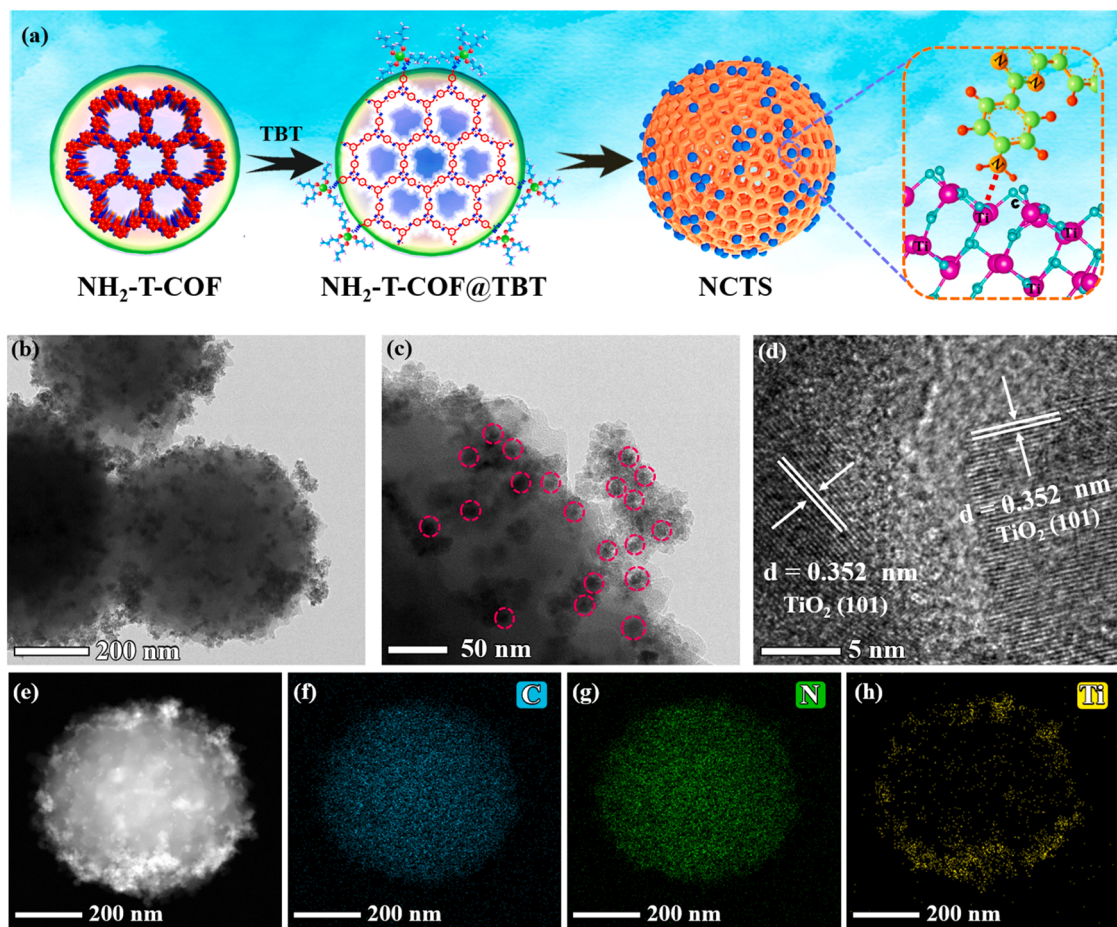


**Fig. 2.** (a) Schematic illustration of the preparation of NCTS. (b, c) TEM images of NCTS-2. (d) HRTEM image and lattice fringes of NCTS-2. (e) The HAADF-TEM image of NCTS-2. (f-h) EDX elemental mapping of NCTS-2.

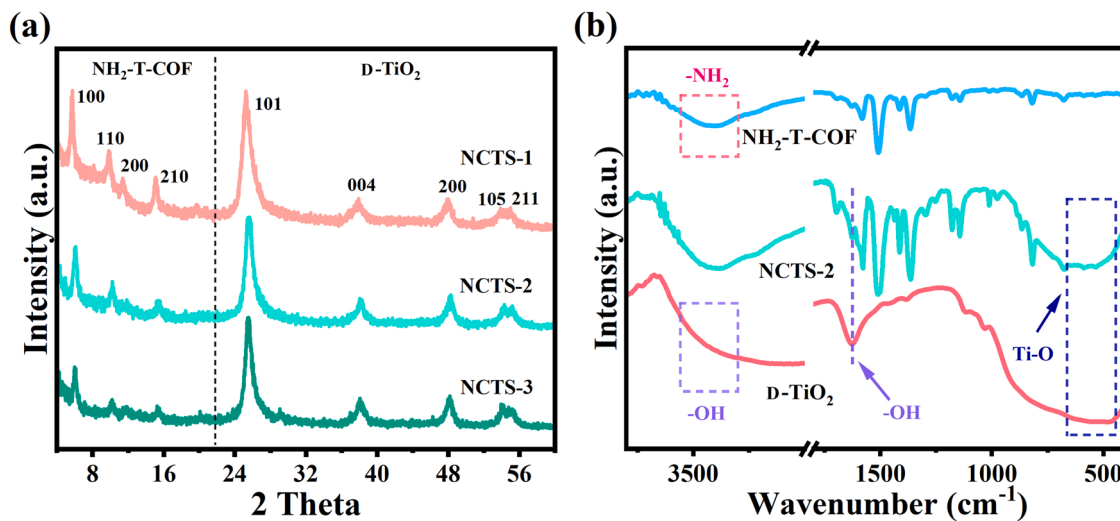


**Fig. 3.** (a) PXRD patterns of NCTS. (b) FT-IR spectra of NCTS-2, NH<sub>2</sub>-T-COF and d-TiO<sub>2</sub>.

NMR spectra of NCTS-2, which further proves that NH<sub>2</sub>-T-COF was not hydrolyzed and the structure is stable after loading defect TiO<sub>2</sub>.

The porosity features of these samples were evaluated by N<sub>2</sub> adsorption and desorption isotherms at 77 K (Fig. 4a). Brunauer–Emmett–Teller (BET) surface area of NCTS-2 was calculated to be 488.7 m<sup>2</sup> g<sup>-1</sup>, smaller than that of pure NH<sub>2</sub>-T-COF (697.8 m<sup>2</sup> g<sup>-1</sup>) due to the presence of d-TiO<sub>2</sub> with a low surface area (256.3 m<sup>2</sup> g<sup>-1</sup>). The

pore size of pure NH<sub>2</sub>-T-COF distributes at around 1.13 nm (Fig. 4b), which was further fitted by nonlocal density functional theory (NLDFT). And the average pore size distributions of NCTS-2 are centered at 3.12 nm because of the introduction of d-TiO<sub>2</sub> with mesoporous (3.61 nm). The plentiful porous structure offers great opportunity for the CO<sub>2</sub> molecules entering the pores and the exposed inner surface where the redox reactions occur. Furthermore, the d-TiO<sub>2</sub> mass content

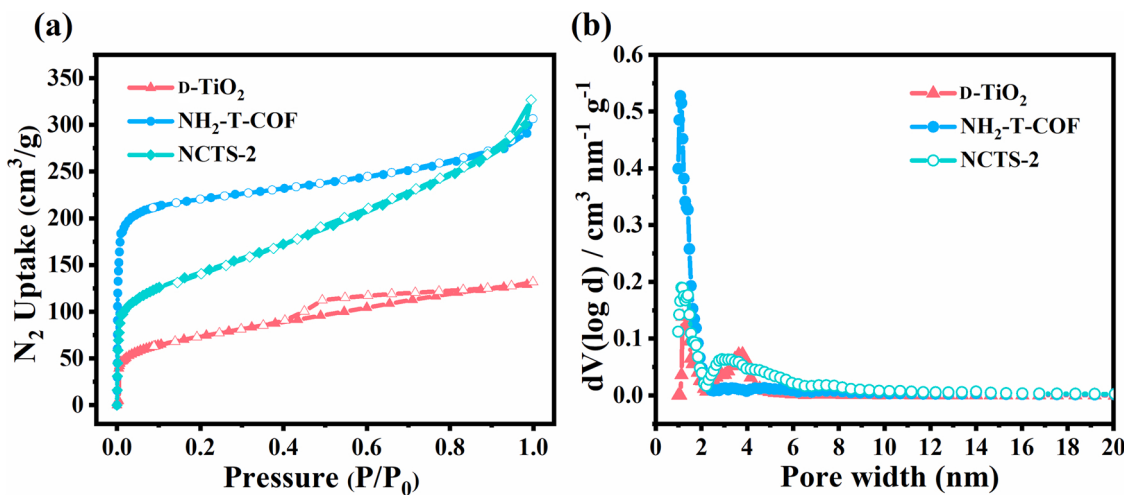


**Fig. 4.** (a)  $N_2$  adsorption (solid symbols) and desorption (open symbols) isotherms of d-TiO<sub>2</sub>, NH<sub>2</sub>-T-COF and NCTS-2 at 77 K. (b) Pore size distribution profiles of d-TiO<sub>2</sub>, NH<sub>2</sub>-T-COF and NCTS-2.

of NCTS composite was investigated from inductively coupled plasma-optical emission spectrometry (ICP-OES) measurement and listed as Table S2. The content of d-TiO<sub>2</sub> in the NCTS-1, NCTS-2 and NCTS-3 composites was calculated to be 16 %, 23 % and 32.2 %, respectively, consistent with the theoretical results. These results indicate that the d-TiO<sub>2</sub> semiconductors are tightly inlayed over the framework of NH<sub>2</sub>-T-COF, confirming the feasibility of this strategy.

### 3.3. Electronic structure and interaction of NH<sub>2</sub>-T-COF/d-TiO<sub>2</sub> heterostructure

The chemical compositions and states of the samples were tested by X-ray photoelectron spectroscopy (XPS). For N 1s spectra of NH<sub>2</sub>-T-COF (Fig. S10), the peak at ~398.2 eV could be ascribed to sp<sup>2</sup> hybridized N (C=N=C), while the peak at ~401.6 eV belongs to the amino groups (C—N—H) on the surface of NH<sub>2</sub>-T-COF sphere. Compare to NH<sub>2</sub>-T-COF, the N 1s spectra of NCTS-2 composite shows an extra peak at ~397.1 eV (Fig. S11), which is assigned to the formed Ti—N bonding between NH<sub>2</sub>-T-COF and d-TiO<sub>2</sub>. For Ti 2p, as shown in Fig. 5a and S12, two peaks at about ~458.7 and ~464.3 eV are attributed to the Ti<sup>4+</sup> 2p<sub>3/2</sub> and Ti<sup>4+</sup> 2p<sub>1/2</sub>, respectively, while another two peaks at ~457.7 and ~463.2 eV are separately assigned to the Ti<sup>3+</sup> 2p<sub>3/2</sub> and Ti<sup>3+</sup> 2p<sub>1/2</sub>, respectively, suggesting the presence of Ti<sup>3+</sup> defects in TiO<sub>2</sub> crystal structure. The intrinsic defects were further supported by

electron paramagnetic resonance (EPR) spectra. As shown in Fig. 5b, the intensive EPR signal located at  $g = 1.998$  are all observed for d-TiO<sub>2</sub> and NCTS-2, further confirming the successful formation of Ti<sup>3+</sup> defects.

To elucidate the electronic structure and coordination information, X-ray absorption near-edge structure (XANES) and extended X-ray absorption fine structure (EXAFS) at the titanium (Ti) K-edge were performed. Normalized Ti K-edge XANES of Ti-foil, anatase phase TiO<sub>2</sub> (anat-TiO<sub>2</sub>) and NCTS-2 were resolved in Fig. 6a. The relative intensities of peaks as well as the line shape of NCTS-2 is consistent with that of the reference anat-TiO<sub>2</sub>, further indicating that the TiO<sub>2</sub> in the heterostructure composite is anatase type [35]. The three peaks at 4965–4980 eV (labeled A, B, and C in the inset of Fig. 6a) are clearly observed, which can be assigned to the characteristic pre-peaks in the anatase Ti k pre-edge region by most of the experimental and theoretical works [36]. Obviously, the intensity of the pre-peak B of NCTS-2 is relatively lower than that of anat-TiO<sub>2</sub>, suggesting that the average oxidation state of the Ti<sup>4+</sup> species of NCTS-2 decreased. The results display that Ti<sup>4+</sup> is partially reduced and formed Ti<sup>3+</sup> defects during solvothermal processes [35–37], which is consistent with the XPS and EPR results. Then, Fourier transform (FT) of EXAFS spectrum in R-space at the Ti K-edge is further presented to provide coordination information (Fig. 6b). Compared with anat-TiO<sub>2</sub>, the first peak of NCTS-2 shifts negatively, which is thought to correspond to the formation of Ti—N bonds.

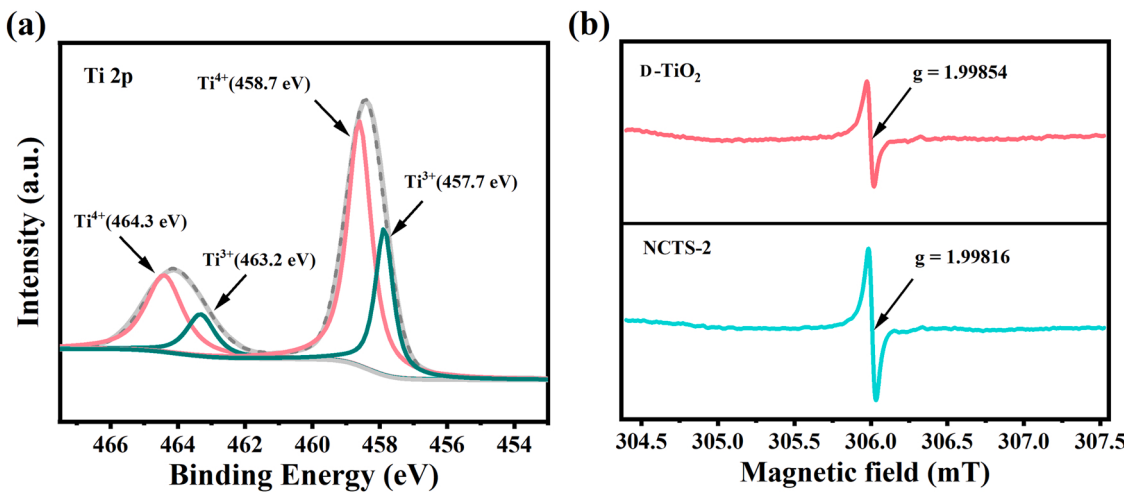


**Fig. 5.** (a) The Ti 2p XPS spectrum of NCTS-2. (b) EPR spectra of d-TiO<sub>2</sub> and NCTS-2.

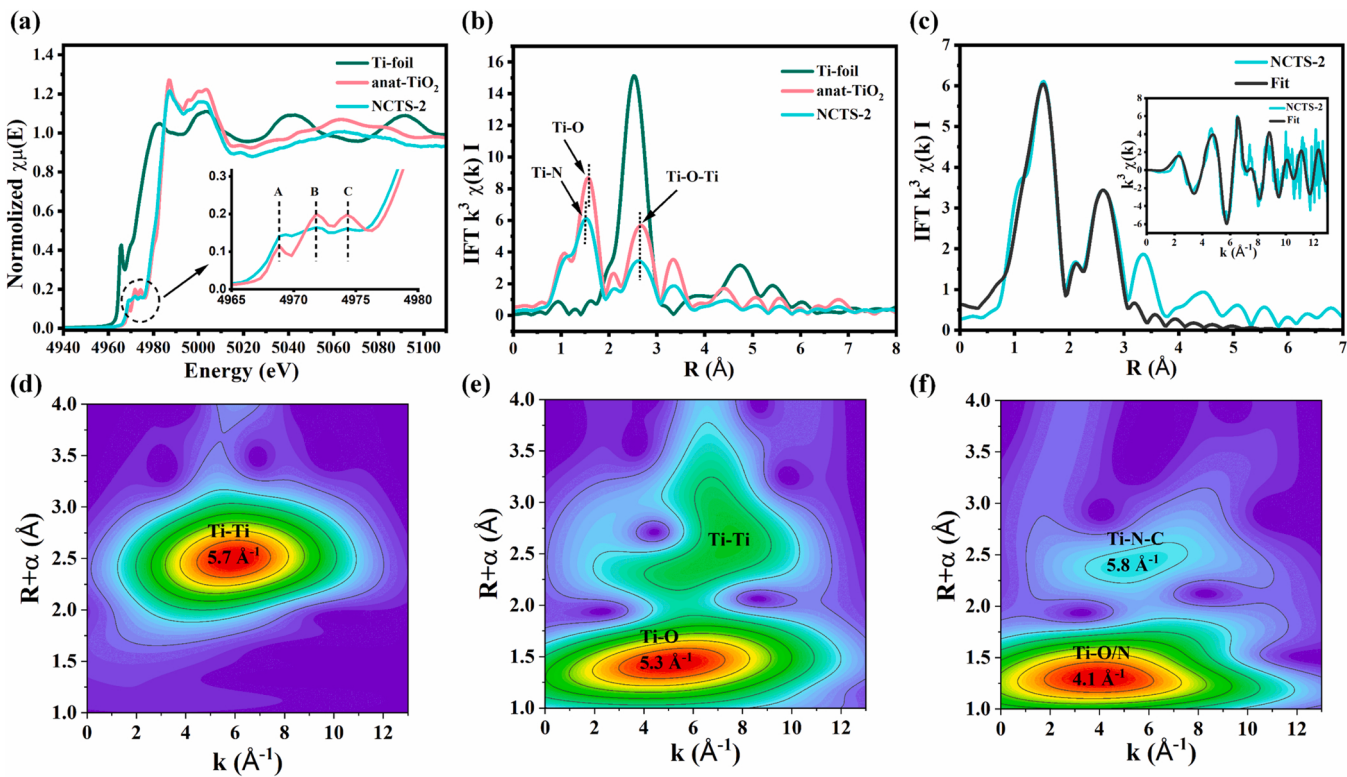


**Fig. 6.** (a) XANES spectra at the Ti K-edge of NCTS-2 sample, anat-TiO<sub>2</sub> and Ti-foil. (b) Fourier transform (FT) at the Ti K-edge of NCTS-2 sample, anat-TiO<sub>2</sub> and Ti-foil. (c) Corresponding EXAFS fitting curves of NCTS-2 at R space and (inset) k space. (d-f) Wavelet transform (WT) of Ti-foil, anat-TiO<sub>2</sub> and NCTS-2 sample.

To confirm the coordination information of Ti throughout the heterostructure NCTS-2, wavelet transform (WT) of Ti K-edge EXAFS oscillations was performed. From the WT contour plots of Ti-foil and anat-TiO<sub>2</sub> (Figs. 6d and 6e), it can be observed that the intensity maxima at 5.7 Å<sup>-1</sup> and 5.3 Å<sup>-1</sup> is associated with the Ti–Ti and T–O contribution, respectively. The WT contour plot of NCTS-2 (Fig. 6f) displays one maximum intensity at 4.1 Å<sup>-1</sup> and one at 5.8 Å<sup>-1</sup>, which can be ascribed to the Ti–O/N first coordination shell and Ti–N–C second coordination shell, respectively [36,38]. EXAFS fitting was performed to extract the structural parameters of Ti atoms (Fig. 6c). The obtained coordination number of the center atom Ti is about 6 (Table S3), owing to the contribution N and O atoms. These results indicate that d-TiO<sub>2</sub> was firmly riveted on the NH<sub>2</sub>–T–COF framework by the coordination with N atoms, as a result of stable heterostructure with strong interfacial interactions between d-TiO<sub>2</sub> and NH<sub>2</sub>–T–COF.

### 3.4. Band structure and Z-scheme charge-transfer behaviors

The light-harvesting capability and electronic band structure of the samples were investigated by UV-vis diffuse reflectance spectroscopy (DRS) and Mott–Schottky measurement. As shown in Fig. 7a and S13, d-TiO<sub>2</sub>, NH<sub>2</sub>–T–COF and NCTS-2 exhibit sharp absorption edges at about 400, 470, and 465 nm, respectively. Compared to d-TiO<sub>2</sub>, the absorption edge of all NCTS samples undergoes an obvious red shift and extends to the visible light region, which was initiated by the incorporation of NH<sub>2</sub>–T–COF. Based on Tauc plot (Fig. S14) [5], the band gap values ( $E_g$ ) of d-TiO<sub>2</sub> and NH<sub>2</sub>–T–COF are estimated to be about 3.10 and 2.65 eV, respectively. Mott–Schottky (MS) measurements were conducted to determine the flat band potential of the samples (Fig. S15) [39]. The flat band potential of d-TiO<sub>2</sub> and NH<sub>2</sub>–T–COF are determined as –0.05 and –0.40 V (vs. RHE). Namely, the conduction band (CB) position of d-TiO<sub>2</sub> and NH<sub>2</sub>–T–COF can be roughly estimated as –0.25 and –0.60 V (vs. RHE) [40]. Combined with the  $E_g$  value of d-TiO<sub>2</sub> and NH<sub>2</sub>–T–COF from UV/Vis DRS plot, the valence band (VB) position of

them can be evaluated as 2.85 and 2.05 V (vs. RHE) and outlined in Fig. 7b.

The work function (WF) was performed to estimate the charge transfer direction at the interface of the heterostructure consisted of d-TiO<sub>2</sub> and NH<sub>2</sub>–T–COF. As illustrated in Figs. 7c and 7d, the work function of d-TiO<sub>2</sub> and NH<sub>2</sub>–T–COF are 5.10 and 4.85 eV, respectively (Fig. S16), that is, the Fermi level (FL) of d-TiO<sub>2</sub> is lower than that of NH<sub>2</sub>–T–COF, which indicates that the electrons on NH<sub>2</sub>–T–COF will flow to d-TiO<sub>2</sub> until their Fermi level reaches equilibrium state after the formation of heterostructure composite. Then the built-in electric field is formed with the direction from NH<sub>2</sub>–T–COF to d-TiO<sub>2</sub> at the interface. Since the direction of the photo-generated electric field is opposite to that of the built-in electric field, when light illuminated, the photoexcited electrons located on the CB of d-TiO<sub>2</sub> will recombine with the holes on the VB of NH<sub>2</sub>–T–COF, forming a Z-scheme charge transfer process at the heterojunction interface between NH<sub>2</sub>–T–COF and d-TiO<sub>2</sub>.

The charge transfer pathway is shown in Fig. 7g and further validated by spin-trapping electron spin resonance (ESR) spectra. We utilized 5,5-dimethyl-l-pyrroline N-oxide (DMPO) to probe the formation of hydroxyl radical (·OH) and superoxide radical (·O<sub>2</sub><sup>−</sup>). As Figs. 7e and 7f show, under the illumination of Xenon lamp for 5 min, the typical peaks of DMPO–OH spin adduct with 1:2:2:1 quadruple signal can be obviously observed in the spectra of d-TiO<sub>2</sub>, while the peaks intensity of DMPO–O<sub>2</sub><sup>−</sup> spin adduct are very weak. The result indicates that d-TiO<sub>2</sub> favors the generation of hydroxyl radical (·OH) rather than superoxide radical (·O<sub>2</sub><sup>−</sup>), which ascribes its more positive VB potential (2.85 V) than that of H<sub>2</sub>O/·OH (1.9 V, pH = 7) [41]. For pristine NH<sub>2</sub>–T–COF photocatalytic system, the characteristic signal of DMPO–O<sub>2</sub><sup>−</sup> spin adduct can be clearly observed, whereas the signal of DMPO–OH is almost undetectable, manifesting that the pure NH<sub>2</sub>–T–COF is favorable for producing ·O<sub>2</sub><sup>−</sup> rather than ·OH radical due to its more negative CB potential than that of O<sub>2</sub>/·O<sub>2</sub><sup>−</sup> (0.33 V) [42,43]. For the heterostructure composite NCTS-2 consisted of d-TiO<sub>2</sub> and NH<sub>2</sub>–T–COF, both signals of DMPO–OH and DMPO–O<sub>2</sub><sup>−</sup> adducts are significantly enhanced than

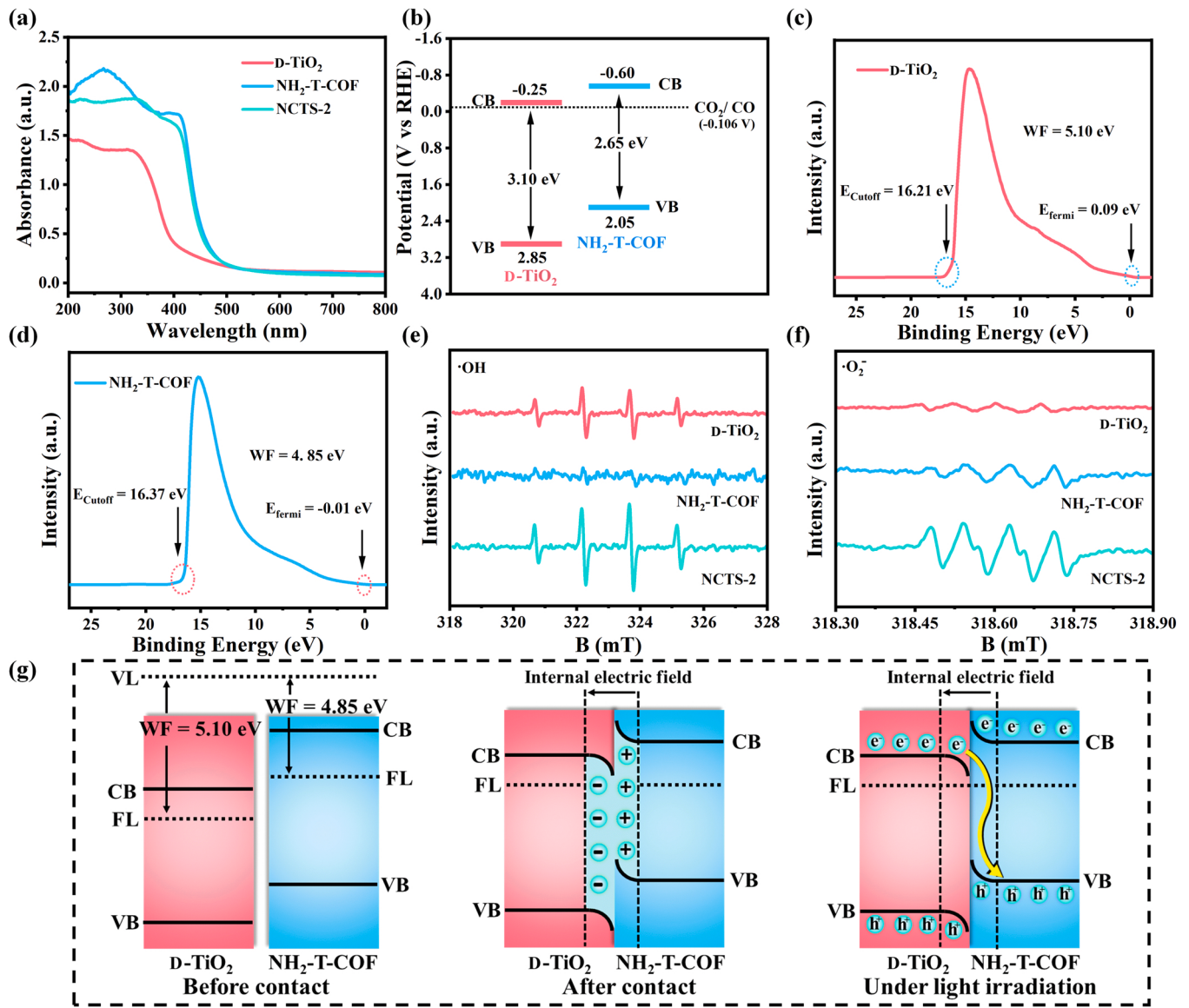


**Fig. 7.** (a) UV–visible DRS spectra of d-TiO<sub>2</sub>, NH<sub>2</sub>-T-COF and NCTS-2. (b) The estimated band structure of d-TiO<sub>2</sub> and NH<sub>2</sub>-T-COF. UPS spectra of (c) d-TiO<sub>2</sub> and (d) NH<sub>2</sub>-T-COF. DMPO spin-trapping ESR spectra recorded for (e) ·OH and (f) ·O<sup>2-</sup> under light irradiation for d-TiO<sub>2</sub>, NH<sub>2</sub>-T-COF and NCTS-2. (g) Schematic illustration of the relative band positions and charge transfer process of d-TiO<sub>2</sub> and NH<sub>2</sub>-T-COF before contact, after contact and under light irradiation.

those of pure d-TiO<sub>2</sub> and NH<sub>2</sub>-T-COF, which reveals that NCTS-2 owns both the strong oxidation ability of d-TiO<sub>2</sub> and the reduction property of NH<sub>2</sub>-T-COF. These results indicate that the photogenerated electrons and holes of NCTS-2 are spatially separated on the semiconductors with higher reduction potential and oxidation potential, respectively, resulting in the Z-scheme migration path of photoelectrons. Moreover, high-resolution *in situ* X-ray photoelectron spectroscopy (XPS) spectra show that under light irradiation, the binding energy of Ti 2p shifts positively compared to that in the dark, whereas the binding energy of N 1 s shows a negatively shift (Fig. S17), which demonstrates that the excited electrons transfer from d-TiO<sub>2</sub> to NH<sub>2</sub>-T-COF under illumination, further proving a Z-scheme charge-transfer path at the interface of NCTS-2 heterostructure. Therefore, under light irradiation, the electrons clustered at the CB of d-TiO<sub>2</sub> can recombine with the holes accumulated in the VB of NH<sub>2</sub>-T-COF via a tight chemical bonding and stable interface, then the electrons and holes with higher reduction potential and oxidation potential can be well-preserved to participate in the redox reactions.

The interfacial Z-scheme charge-transfer behavior was further

measured by photoluminescence spectra (PL) and photoelectrochemical measurements. As the PL spectra shows in Fig. S18, the emission intensity observed from NCTS-2 is much weaker than that of d-TiO<sub>2</sub> and NH<sub>2</sub>-T-COF, indicative of the low recombination rate of photoexcited electron-hole pairs after formation of the Z-scheme heterostructure. To explore the effect of interfacial interaction of the heterostructure on charge-transfer behavior, the NCTS-2 counterpart consisting of defect-free TiO<sub>2</sub> and NH<sub>2</sub>-T-COF (defect-free NCTS-2) was synthesized (Fig. S19). As depicted in Fig. 8a, the transient photocurrent response of NCTS-2 exhibits a significantly enhancement of photocurrent intensity compared to pure d-TiO<sub>2</sub> and NH<sub>2</sub>-T-COF, suggesting its greatly improved separation/transfer efficiency of the photogenerated electrons/holes after the constitution of heterojunction composite. Significantly, the photocurrent intensity of NCTS-2 is much higher than that of defect-free NCTS-2, which suggests that the strong interaction between d-TiO<sub>2</sub> and NH<sub>2</sub>-T-COF not only provide a tight and stable interface, but also significantly promote the migration and separation of electrons and holes. Additionally, electrochemical impedance spectroscopy (EIS) displays that NCTS-2 shows the smallest radius of the high-frequency

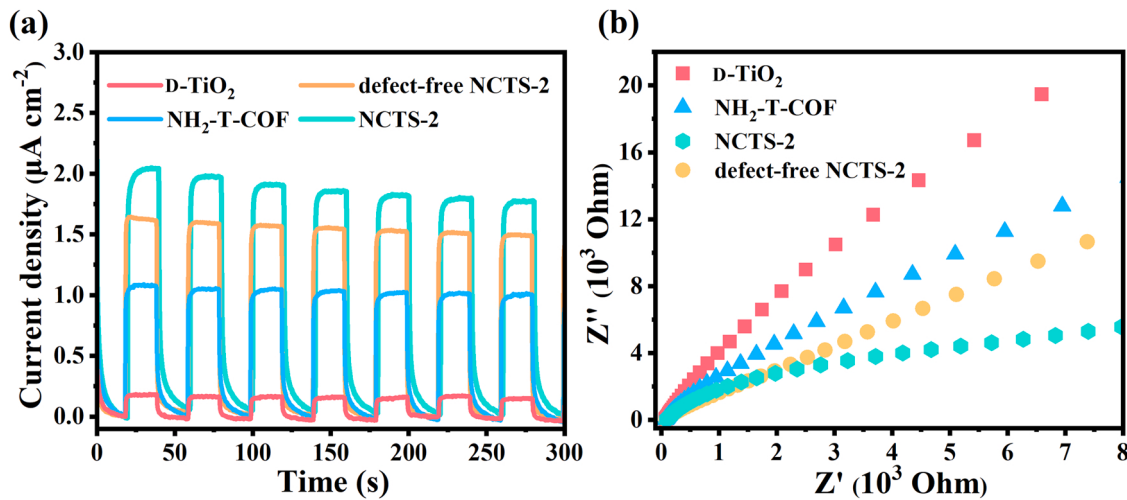


**Fig. 8.** (a) Transient photocurrent responses of d-TiO<sub>2</sub>, NH<sub>2</sub>-T-COF, NCTS-2 and defect-free NCTS-2. (b) Electrochemical impedance spectroscopy of d-TiO<sub>2</sub>, NH<sub>2</sub>-T-COF, NCTS-2 and defect-free NCTS-2.

semicircle with respect to all sample (Fig. 8b), indicating its higher conductivity than that of d-TiO<sub>2</sub>, NH<sub>2</sub>-T-COF and defect-free NCTS-2. These results demonstrate that the charges of NCTS-2 can be separated and transported in a Z-scheme route through the robust Ti–N bonding between d-TiO<sub>2</sub> and NH<sub>2</sub>-T-COF, remaining the charges with higher redox capacity to participate the reaction. And compared to defect-free NCTS-2, the strong chemical bond connection between d-TiO<sub>2</sub> and NH<sub>2</sub>-T-COF can remarkably improve the charge separation efficiency, providing more opportunities for photogenerated charges to drive redox reaction.

### 3.5. Photocatalytic CO<sub>2</sub>RR performance

The photocatalytic CO<sub>2</sub> reduction reaction (CO<sub>2</sub>RR) performance of the photocatalysts was performed in a closed gas circulation system and evaluated under pure CO<sub>2</sub> (0.8 bar, 298 K) atmosphere in acetonitrile/water (5:3) mixture with ascorbic acid as sacrificial agent. Previous studies have confirmed that the CO<sub>2</sub> adsorption ability is beneficial to the improvement of the photocatalytic CO<sub>2</sub>RR performance. The CO<sub>2</sub> adsorption isotherms were performed for the hybrid material NCTS-2, pure d-TiO<sub>2</sub> and NH<sub>2</sub>-T-COF. As shown in Fig. 9a, NCTS-2 has a substantially improvement of CO<sub>2</sub> adsorption with an uptake of 58.1  $\text{cm}^{-1} \text{ g}^{-1}$  compared to pristine d-TiO<sub>2</sub> (11.1  $\text{cm}^{-1} \text{ g}^{-1}$ ), attributing to the strong affinity between the rich-N groups in the framework of NH<sub>2</sub>-T-COF and CO<sub>2</sub> molecules. The increased CO<sub>2</sub> adsorption capacity of NCTS-2 complex is kinetically advantageous for CO<sub>2</sub> reduction. As expected, after 4 h of light irradiation, the NCTS-2 generated a maximum amount of CO of 7.51  $\mu\text{mol}$ , that is 9.3 times than that of pure d-TiO<sub>2</sub> (0.81  $\mu\text{mol}$ ) (Fig. 9b). Notably, d-TiO<sub>2</sub> produces a large amount of by-product H<sub>2</sub> during the progress of photocatalytic CO<sub>2</sub>RR, while H<sub>2</sub> is hardly detected in the system of NCTS-2. In detail, the selectivity of pure d-TiO<sub>2</sub> to generate CO is only 15 %, but that of NCTS-2 composite is as high as nearly 100 %, which may give the credit to the substantial increase of CO<sub>2</sub> concentration at the reaction site. The kinetic curve of CO formation is shown in Fig. 9c and S20, all the NCTS hybrid samples display a significantly improved photocatalytic activity for CO evolution compared to pure d-TiO<sub>2</sub> and NH<sub>2</sub>-T-COF. As the increase of d-TiO<sub>2</sub> on the surface of the NH<sub>2</sub>-T-COF sphere, the activity of NCTS-3 shows a decreasing trend. This may be due to the fact that excess d-TiO<sub>2</sub> will reduce the light-harvesting capability of NH<sub>2</sub>-T-COF as well as destroy its crystallinity. The poor crystallinity would be detrimental to the fast transfer of photoexcited electrons and holes, resulting in a decrease in the photocatalytic activity. By optimizing the loading of the precursor tetrabutyl titanate, the resultant NCTS-2 with 23% TiO<sub>2</sub> delivers the

highest photocatalytic CO<sub>2</sub>RR performance. Notably, the CO formation rate of NCTS-2 is also faster than that of defect-free NCTS-2, indicating that the strong interfacial interactions and intimate contact interface between two semiconductors is very significant for the photocatalytic performance of heterostructure photocatalyst. To provide a reference for different comparison, the rates of CO evolution per gram of NCTS-2, d-TiO<sub>2</sub> and NH<sub>2</sub>-T-COF are listed as Fig. S21.

The apparent quantum yield (AQY) is a significant parameter to evaluate the performance of photocatalyst.[44] The AQY for photocatalytic CO evolution of NCTS-2, d-TiO<sub>2</sub> and NH<sub>2</sub>-T-COF were measured under the same reaction conditions but with different monochromatic light. The wavelength dependent AQY values are depicted as Fig. 9d, the AQY value of NCTS-2 was calculated to 1.41 % and 0.40 % at 365 nm and 420 nm, respectively. Moreover, the AQY value largely depends on the photocatalyst weight [45]. By optimization of the photocatalyst mass (Fig. 9e), the AQY value of NCTS-2 reaches 6.81 % at 365 nm, about 9 and 8 times better than that of pure d-TiO<sub>2</sub> (0.74%) and NH<sub>2</sub>-T-COF (0.83 %). Since the framework of COF and solvent also contain a large amount of carbon element, the isotope labeling experiment was performed to validate the carbon source of the resulting product originated from the photocatalytic CO<sub>2</sub>RR process. We employed isotope-labeled carbon dioxide (<sup>13</sup>CO<sub>2</sub>) as an alternative source gas with NCTS-2 sample to complete the evaluation experiment. As shown in the mass spectra in Fig. 9f, <sup>13</sup>CO ( $m/z = 29$ ) was finally detected, which proves that the generated CO originates from the reactant CO<sub>2</sub> rather than the decomposition of photocatalyst and solvent. Additionally, NCTS-2 photocatalyst ran for 24 h or 5 cycles, but its activity did not decrease significantly. (Fig. 9g and Fig. S22). The structural integrity and crystallinity of NCTS-2 retain after the long-term reaction, as proved by PXRD pattern and Roman spectra (Fig. 9h and i).

### 3.6. Mechanism of the activity enhancement

To further understand the mechanisms for photocatalytic CO<sub>2</sub>RR on the catalysts, *in situ* diffuse reflectance infrared Fourier transform spectra (DRIFTS) was conducted to investigate the processes of CO<sub>2</sub> adsorption and activation on NCTS-2 and d-TiO<sub>2</sub>. CO<sub>2</sub> can either act as a linear molecule, physically adsorbed on the catalyst surface, or as a bent molecule, chemisorbed on the catalyst surface. As shown in Figs. 10a and 10b, the DRIFTS of CO<sub>2</sub> adsorbed on both NCTS-2 and d-TiO<sub>2</sub> show two physisorption peaks at  $\sim 2363$  and  $\sim 2338 \text{ cm}^{-1}$  [46]. Note that the intensity of the peaks for NCTS-2 is obviously higher than d-TiO<sub>2</sub>, indicating that the adsorption capacity of NCTS-2 for CO<sub>2</sub> is significantly enhanced owing to the introduction of rich-N NH<sub>2</sub>-T-COF. CO<sub>2</sub>

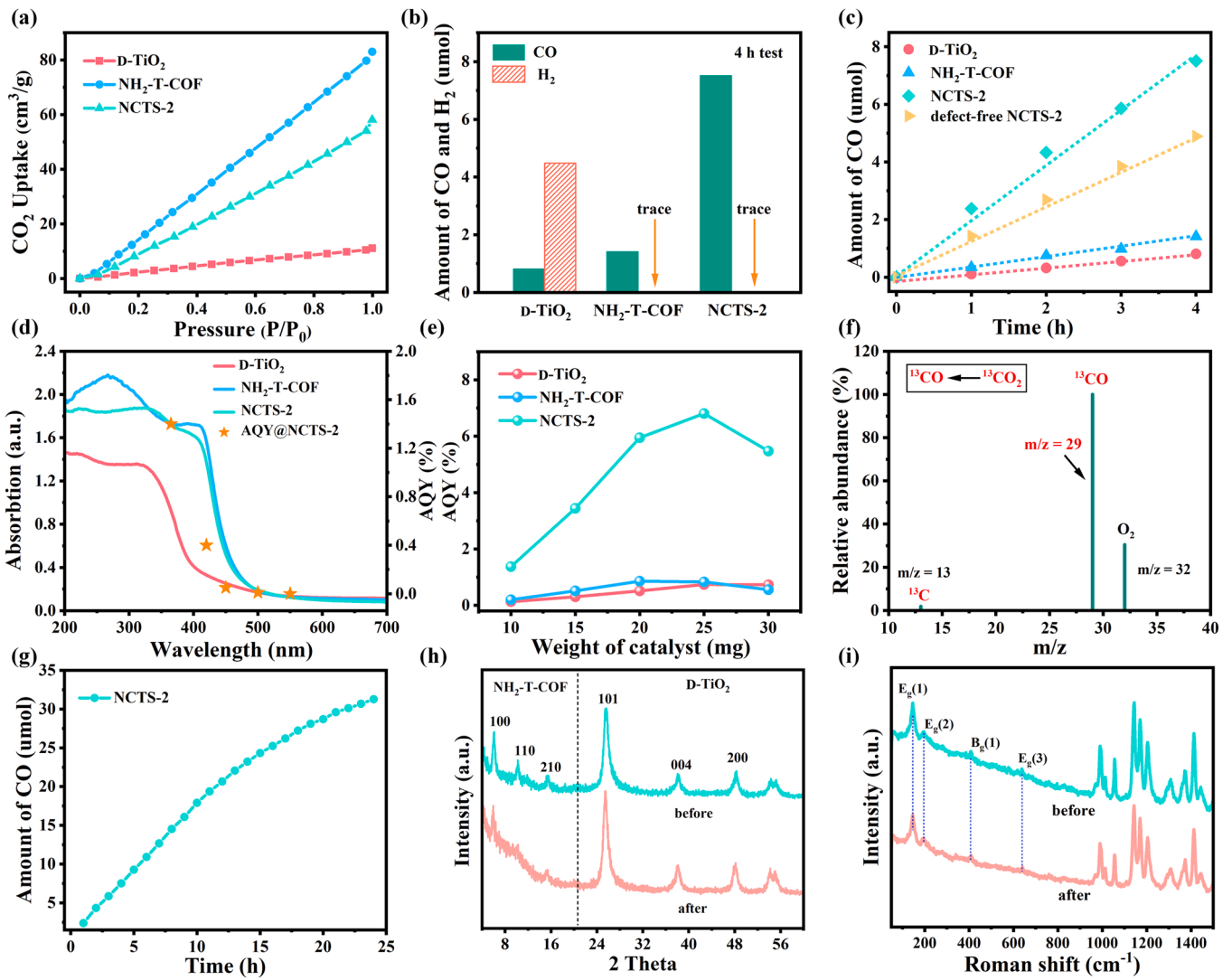


**Fig. 9.** (a) CO<sub>2</sub> adsorption curves of d-TiO<sub>2</sub>, NH<sub>2</sub>-T-COF and NCTS-2 measured at 273 K. (b) Photocatalytic CO<sub>2</sub>RR performance of d-TiO<sub>2</sub>, NH<sub>2</sub>-T-COF and NCTS-2. (c) Time-dependent CO production performance using d-TiO<sub>2</sub>, NH<sub>2</sub>-T-COF, NCTS-2 and defect-free NCTS-2 as photocatalyst. (d) AQY values of NCTS-2 (10 mg) under different monochromatic light irradiation and UV/Vis DRS plot. (e) AQY values of d-TiO<sub>2</sub>, NH<sub>2</sub>-T-COF and NCTS-2 at different photocatalyst weights under 365 nm. (f) Mass spectra of <sup>13</sup>CO produced from the photocatalytic reduction of <sup>13</sup>CO<sub>2</sub> over NCTS-2. (g) Photocatalytic durability test of NCTS-2. (h) PXRD pattern and (i) Raman spectra of NCTS-2 before and after photocatalytic CO<sub>2</sub>RR.

chemisorption results in the formation of partially charged CO<sub>2</sub><sup>δ-</sup> species through interactions with surface atoms of catalyst [47]. As depicted in Fig. 10c, the chemisorption peak at ~1517 cm<sup>-1</sup> corresponds to monodentate carbonate (m-CO<sub>3</sub><sup>2-</sup>), and those at 1328 and 1590 cm<sup>-1</sup> assign to bidentate carbonate (b-CO<sub>3</sub><sup>2-</sup>), while d-TiO<sub>2</sub> has only the signal of m-CO<sub>3</sub><sup>2-</sup>, but no signal of b-CO<sub>3</sub><sup>2-</sup> (Fig. 10d) [13, 46, 48]. For d-TiO<sub>2</sub>, the presence of m-CO<sub>3</sub><sup>2-</sup> signal indicates that the Type I CO<sub>2</sub> adsorption mode (Fig. 10e) can be formed on the surface of d-TiO<sub>2</sub>, due to the interaction between carbon atom of the CO<sub>2</sub> molecule and titanium/oxygen atoms on the surface of d-TiO<sub>2</sub>. For NCTS-2 composite, the appearance of b-CO<sub>3</sub><sup>2-</sup> signals manifests that Type II, Type III and Type IV CO<sub>2</sub> adsorption modes may coexist [47, 49, 50]. However, the oxygen coordination mode (Type II and Type III) has been proved that the final product is formic acid (HCOOH) rather than carbon monoxide (CO) because the breaking of the C–O bond in the CO<sub>2</sub> molecule does not occur in this situation [51]. As for the carbon (Type I) or mixed coordination mode (Type IV), the anchoring of the carbon atom on the surface of catalyst makes them difficult to undergo hydrogenation and is more favored to produce CO [51]. Therefore, the mixed coordination mode (Type IV) is the main adsorbed CO<sub>2</sub><sup>δ-</sup> species on the surface of

NCTS-2, due to the synergistic adsorption and activation for CO<sub>2</sub> molecule through the nitrogen atoms of NH<sub>2</sub>-T-COF framework and the titanium/oxygen atoms of d-TiO<sub>2</sub>. Both NCTS-2 and d-TiO<sub>2</sub> show the bicarbonate (HCO<sub>3</sub><sup>-</sup>) signals due to the interaction of hydroxyl groups on the surface of sample with CO<sub>2</sub> molecules. All these carbonate and bicarbonate species are bent to lose the linear symmetry of free CO<sub>2</sub> molecules, then achieve further activation by accepting electrons. The peaks at about 1607 and 1248–1278 cm<sup>-1</sup> are attributed to ·CO<sub>2</sub><sup>-</sup> intermediates, indicating that the adsorbed CO<sub>2</sub> molecules can be successfully activated on the surface of NCTS-2 and d-TiO<sub>2</sub>, and then transform into product CO [48, 52, 53].

Compared to d-TiO<sub>2</sub>, the introduction of amine-functionalized COF provides more adsorption and activation sites for CO<sub>2</sub>, which is important for suppressing the competitive HER to increase the selectivity towards CO product of NCTS-2 photocatalyst (Fig. 10f). Moreover, the mixed carbon-oxygen coordination on the surface of NCTS-2 leads to more stable arrangements than the pure carbon coordination on the surface of d-TiO<sub>2</sub>. Thus, the mixed coordination is more energetically favored to achieve further activation to form ·CO<sub>2</sub><sup>-</sup> intermediate that is always considered as the rate-limiting step [49]. Although the formation

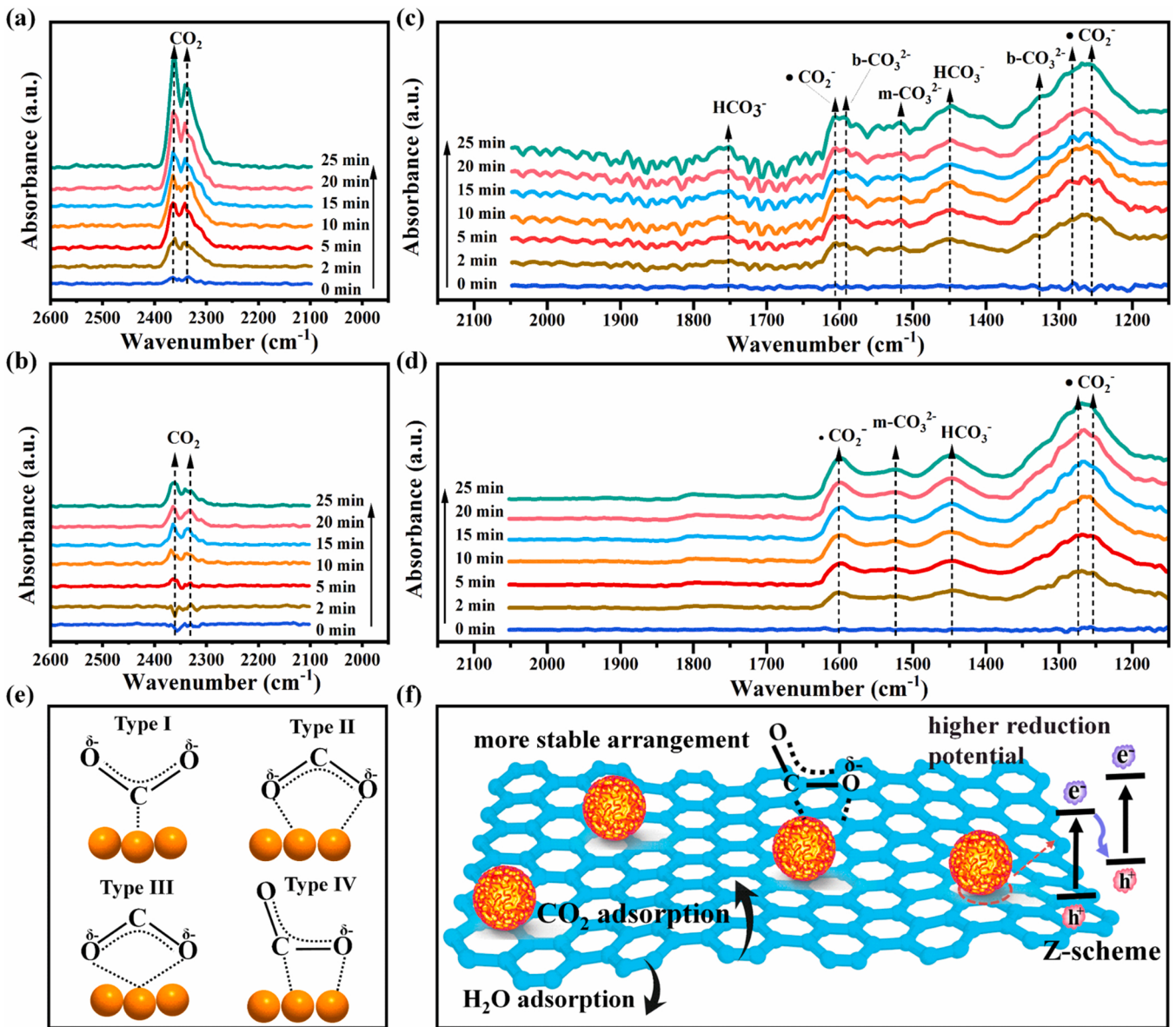


**Fig. 10.** *In situ* DRIFTS measurement of NCTS-2 (a, c) and d-TiO<sub>2</sub> (b, d) in the presence of H<sub>2</sub>O and CO<sub>2</sub> under constant simulated solar illumination. (e) The possible adsorbed CO<sub>2</sub><sup>δ-</sup> species on d-TiO<sub>2</sub> and NCTS-2. (f) Schematic diagram of important reasons for the excellent photocatalytic CO<sub>2</sub>RR performance of NCTS-2 heterostructure.

of the bent CO<sub>2</sub><sup>δ-</sup> species can reduce the overpotential to form •CO<sub>2</sub> intermediate, the formation of both •CO<sub>2</sub> intermediate and CO still requires sufficient driving force from photogenerated electrons to achieve. NCTS-2 as Z-scheme heterostructure, the photogenerated electrons with higher reduction potential are preserved, so NCTS-2 has more driving force to carry out the one-electron reduction of CO<sub>2</sub> to •CO<sub>2</sub> (or •CO<sub>2</sub> to CO) than pure d-TiO<sub>2</sub>. Based on the above discussion, a possible mechanism of the CO<sub>2</sub> reduction over NCTS-2 is proposed. The •CO<sub>2</sub> intermediate obtained by CO<sub>2</sub> adsorption and activation is bound to N/Ti atoms of NCTS-2 through the carbon atom. The oxygen atom in •CO<sub>2</sub> would combine with a hydrogen atom to form the carboxyl radical. The process of bonding hydrogen would lead to breaking the bond between this oxygen atom and the carbon atom and then disintegrates into the carbon monoxide.

#### 4. Conclusions

In summary, we present a theory-guided design of a stable COF-

based Z-scheme heterostructure with well-engineered geometry configuration and intimate contact interface by *in situ* anchoring defect TiO<sub>2</sub> on the surface of amine-functionalized T-COF sphere for photocatalytic CO<sub>2</sub> reduction. EPR spectra combining XPS results and Ti K-edge EXAFS prove the successful formation of Ti<sup>3+</sup> defects and the presence of N-Ti chemical bonding. The Ti-N bonding between d-TiO<sub>2</sub> and NH<sub>2</sub>-T-COF not only results in a well-combined interface, but also acts as a good electrons delivery channel between them, forming a Z-scheme heterostructure with a low charge transfer resistance. The designed NCTS-2 heterostructure photocatalyst displays an excellent activity and selectivity for photocatalytic CO<sub>2</sub> reduction to CO. Compared to pure d-TiO<sub>2</sub>, the significantly enhanced photocatalytic activity and selectivity of NCTS-2 attribute to following aspects: i) the introduction of amine-functionalized COF provides more adsorption and activation sites for CO<sub>2</sub>; ii) the synergistic effect of Ti sites and rich-N groups of NH<sub>2</sub>-T-COF framework energetically favors to form •CO<sub>2</sub> intermediate that is always considered as the rate-limiting step; and iii) NCTS-2 as Z-scheme heterostructure possesses higher reduction

potential to drive the reduction of CO<sub>2</sub> to CO. Our finding would provide useful guidance to design and fabricate the stable COF-based Z-scheme heterostructure with well-defined geometry configuration, intimate contact interface and good electron delivery channel for photocatalysis research.

## CRediT authorship contribution statement

**Y. Wang:** Conceptualization, methodology, investigation, formal analysis, writing-original draft, and writing-review & editing. **Z. Hu:** Data curation and formal analysis. **W. Wang and Y. Li:** Data curation and software. **H. He:** Methodology and formal analysis. **L. Deng:** Supervision, conceptualization, methodology, writing-original draft, and writing-review & editing. **Y. Zhang, J. Huang, N. Zhao and G. Yu:** Methodology and formal analysis. **Y.-N. Liu:** Supervision, conceptualization, funding acquisition, writing-original draft, and writing-review & editing.

## Declaration of Competing Interest

The authors declare that they have no known competing financial interests or personal relationships that could have appeared to influence the work reported in this paper.

## Data availability

Data will be made available on request.

## Acknowledgments

This work was supported by the National Natural Science Foundation of China (No. 22238013 and 22178393), the Foundation of State Key Laboratory of Coal Conversion, Shanxi, China (Grant No. J21-22-609), and the Hunan Provincial Science and Technology Plan Project, China (No. 2019TP1001 and 2020JJ3044). Yan Wang acknowledges the financial support from Fundamental Research Funds for the Central Universities of Central South University (2022ZZTS0303).

## Appendix A. Supporting information

Supplementary data associated with this article can be found in the online version at [doi:10.1016/j.apcatb.2023.122419](https://doi.org/10.1016/j.apcatb.2023.122419).

## References

- [1] C. Xu, P. Ravi Anusuyadevi, C. Aymonier, R. Luque, S. Marre, Nanostructured materials for photocatalysis, *Chem. Soc. Rev.* 48 (2019) 3868–3902, <https://doi.org/10.1039/c9cs00102f>.
- [2] C. Bie, L. Wang, J. Yu, Challenges for photocatalytic overall water splitting, *Chem* 8 (2022) 1567–1574, <https://doi.org/10.1016/j.chempr.2022.04.013>.
- [3] L. Wang, L. Wang, S. Yuan, L. Song, H. Ren, Y. Xu, M. He, Y. Zhang, H. Wang, Y. Huang, T. Wei, J. Zhang, Y. Himeda, Z. Fan, Covalently-bonded single-site Ru-N<sub>2</sub> knitted into covalent triazine frameworks for boosting photocatalytic CO<sub>2</sub> reduction, *Appl. Catal. B: Environ.* (2022), 122097, <https://doi.org/10.1016/j.apcatb.2022.122097>.
- [4] J. Wang, Y. Yu, J. Cui, X. Li, Y. Zhang, C. Wang, X. Yu, J. Ye, Defective g-C<sub>3</sub>N<sub>4</sub>/covalent organic framework van der Waals heterojunction toward highly efficient S-scheme CO<sub>2</sub> photoreduction, *Appl. Catal. B: Environ.* 301 (2022), 120814, <https://doi.org/10.1016/j.apcatb.2021.120814>.
- [5] R. Chen, Y. Wang, Y. Ma, A. Mal, X.Y. Gao, L. Gao, L. Qiao, X. Li, L. Wu, C. Wang, Rational design of isostructural 2D porphyrin-based covalent organic frameworks for tunable photocatalytic hydrogen evolution, *Nat. Commun.* 12 (2021) 1354, <https://doi.org/10.1038/s41467-021-21527-3>.
- [6] H.L. Nguyen, A. Alzamly, Covalent organic frameworks as emerging platforms for CO<sub>2</sub> photoreduction, *ACS Catal.* 11 (2021) 9809–9824, <https://doi.org/10.1021/acscatal.1c02459>.
- [7] Y. Fu, Y. Liao, P. Li, H. Li, S. Jiang, H. Huang, W. Sun, T. Li, H. Yu, K. Li, H. Li, B. Jia, T. Ma, Layer structured materials for ambient nitrogen fixation, *Coord. Chem. Rev.* 460 (2022), 214468, <https://doi.org/10.1016/j.ccr.2022.214468>.
- [8] Q. Yang, M. Luo, K. Liu, H. Cao, H. Yan, Covalent organic frameworks for photocatalytic applications, *Appl. Catal. B: Environ.* 276 (2020), 119174, <https://doi.org/10.1016/j.apcatb.2020.119174>.
- [9] S. Yang, R. Sa, H. Zhong, H. Lv, D. Yuan, R. Wang, Microenvironments enabled by covalent organic framework linkages for modulating active metal species in photocatalytic CO<sub>2</sub> reduction, *Adv. Funct. Mater.* 32 (2022), <https://doi.org/10.1002/adfm.202110694>.
- [10] L. Zou, R. Sa, H. Zhong, H. Lv, X. Wang, R. Wang, Photoelectron transfer mediated by the interfacial electron effects for boosting visible-light-driven CO<sub>2</sub> reduction, *ACS Catal.* 12 (2022) 3550–3557, <https://doi.org/10.1021/acscatal.1c05449>.
- [11] Y. Liu, W. Zhou, W. Teo, K. Wang, L. Zhang, Y. Zeng, Y. Zhao, Covalent-organic-framework-based composite materials, *Chem* 6 (2020) 3172–3202, <https://doi.org/10.1016/j.chempr.2020.08.021>.
- [12] Y. Cao, W. Sun, C. Guo, L. Zheng, M. Yao, Y. Wang, Rational construction of yolk-shell bimetal-modified quinonyl-rich covalent organic polymers with ultralong lithium-storage mechanism, *ACS Nano* 16 (2022) 9830–9842, <https://doi.org/10.1021/acsnano.2c03857>.
- [13] X. Yang, S. Wang, N. Yang, W. Zhou, P. Wang, K. Jiang, S. Li, H. Song, X. Ding, H. Chen, J. Ye, Oxygen vacancies induced special CO<sub>2</sub> adsorption modes on Bi<sub>2</sub>MoO<sub>6</sub> for highly selective conversion to CH<sub>4</sub>, *Appl. Catal. B: Environ.* 259 (2019), 118088, <https://doi.org/10.1016/j.apcatb.2019.118088>.
- [14] M. Zhang, M. Lu, Z. Lang, J. Liu, M. Liu, J. Chang, L. Li, L. Shang, M. Wang, S. Li, Y. Lan, Semiconductor/covalent-organic-framework Z-scheme heterojunctions for artificial photosynthesis, *Angew. Chem. Int. Ed.* 59 (2020) 6500–6506, <https://doi.org/10.1002/anie.202000929>.
- [15] Y. Xiong, Q. Liao, Z. Huang, X. Huang, C. Ke, H. Zhu, C. Dong, H. Wang, K. Xi, P. Zhan, F. Xu, Y. Lu, Ultrahigh responsivity photodetectors of 2D covalent organic frameworks integrated on graphene, *Adv. Mater.* 32 (2020) 1907242, <https://doi.org/10.1002/adma.201907242>.
- [16] Y. Wang, Z. Hu, W. Wang, H. He, L. Deng, Y. Zhang, J. Huang, N. Zhao, G. Yu, Y.-N. Liu, Design of well-defined shell-core covalent organic frameworks/metal sulfide as an efficient Z-scheme heterojunction for photocatalytic water splitting, *Chem. Sci.* 12 (2021) 16065–16073, <https://doi.org/10.1039/dsc05893b>.
- [17] L. Sun, L. Li, J. Yang, J. Fan, Q. Xu, Fabricating covalent organic framework/CdS S-scheme heterojunctions for improved solar hydrogen generation, *Chin. J. Catal.* 43 (2022) 350–358, [https://doi.org/10.1016/s1872-2067\(21\)63869-x](https://doi.org/10.1016/s1872-2067(21)63869-x).
- [18] J. Liu, Y. Li, J. Ke, S. Wang, L. Wang, H. Xiao, Black NiO-TiO<sub>2</sub> nanorods for solar photocatalysis: Recognition of electronic structure and reaction mechanism, *Appl. Catal. B: Environ.* 224 (2018) 705–714, <https://doi.org/10.1016/j.apcatb.2017.11.028>.
- [19] E.A. Dolgopolova, V.A. Galitskiy, C.R. Martin, H.N. Gregory, B.J. Yarbrough, A. M. Rice, A.A. Berseneva, O.A. Ejegbabwo, K.S. Stephenson, P. Kittikhunnatham, S. G. Karakalos, M.D. Smith, A.B. Greytak, S. Garashchuk, N.B. Shustova, Connecting wires: photoinduced electronic structure modulation in metal-organic frameworks, *J. Am. Chem. Soc.* 141 (2019) 5350–5358, <https://doi.org/10.1021/jacs.8b13853>.
- [20] Y. Zhao, S. Zhang, R. Shi, G.I.N. Waterhouse, J. Tang, T. Zhang, Two-dimensional photocatalyst design: a critical review of recent experimental and computational advances, *Mater. Today* 34 (2020) 78–91, <https://doi.org/10.1016/j.mattod.2019.10.022>.
- [21] J. Jia, C. Qian, Y. Dong, Y. Li, H. Wang, M. Ghoussooub, K.T. Butler, A. Walsh, G. A. Ozin, Heterogeneous catalytic hydrogenation of CO<sub>2</sub> by metal oxides: defect engineering - perfecting imperfection, *Chem. Soc. Rev.* 46 (2017) 4631–4644, <https://doi.org/10.1039/c7cs00026j>.
- [22] Y. Sun, T. Wu, Z. Bao, J. Moon, Z. Huang, Z. Chen, H. Chen, M. Li, Z. Yang, M. Chi, T.J. Toops, Z. Wu, D.E. Jiang, J. Liu, S. Dai, Defect engineering of ceria nanocrystals for enhanced catalysis via a high-entropy oxide strategy, *ACS Cent. Sci.* 8 (2022) 1081–1090, <https://doi.org/10.1021/acscentsci.2c00340>.
- [23] W. Jiang, H. Loh, B.Q.L. Low, H. Zhu, J. Low, J.Z.X. Heng, K.Y. Tang, Z. Li, X. J. Loh, E. Ye, Y. Xiong, Role of oxygen vacancy in metal oxides for photocatalytic CO<sub>2</sub> reduction, *Appl. Catal. B: Environ.* 321 (2023), 122079, <https://doi.org/10.1016/j.apcatb.2022.122079>.
- [24] A. Naldoni, M. Altomare, G. Zoppiello, N. Liu, S. Kment, R. Zboril, P. Schmuki, Photocatalysis with reduced TiO<sub>2</sub>: from black TiO<sub>2</sub> to cocatalyst-free hydrogen production, *ACS Catal.* 9 (2019) 345–364, <https://doi.org/10.1021/acscatal.8b04068>.
- [25] J. Wu, X. Li, W. Shi, P. Ling, Y. Sun, X. Jiao, S. Gao, L. Liang, J. Xu, W. Yan, C. Wang, Y. Xie, Efficient visible-light-driven CO<sub>2</sub> reduction mediated by defect-engineered BiOBr atomic layers, *Angew. Chem. Int. Ed.* 57 (2018) 8719–8723, <https://doi.org/10.1002/anie.201803514>.
- [26] S. Wang, X. Hai, X. Ding, S. Jin, Y. Xiang, P. Wang, B. Jiang, F. Ichihara, M. Oshikiri, X. Meng, Y. Li, W. Matsuda, J. Ma, S. Seki, X. Wang, H. Huang, Y. Wada, H. Chen, J. Ye, Intermolecular cascaded π-conjugation channels for electron delivery powering CO<sub>2</sub> photoreduction, *Nat. Commun.* 11 (2020) 1149, <https://doi.org/10.1038/s41467-020-14851-7>.
- [27] P. Zhou, J. Yu, M. Jaroniec, All-solid-state Z-scheme photocatalytic systems, *Adv. Mater.* 26 (2014) 4920–4935, <https://doi.org/10.1002/adma.201400288>.
- [28] H. Qian, Q. Hou, W. Zhang, Y. Nie, R. Lai, H. Ren, G. Yu, X. Bai, H. Wang, M. Ju, Construction of electron transport channels and oxygen adsorption sites to modulate reactive oxygen species for photocatalytic selective oxidation of 5-hydroxymethylfurfural to 2,5-diformylfuran, *Appl. Catal. B: Environ.* 319 (2022), 121907, <https://doi.org/10.1016/j.apcatb.2022.121907>.
- [29] X. Li, C. Garlis, Q. Guan, S. Anwer, K. Al-Ali, G. Palmisano, L. Zheng, A review of material aspects in developing direct Z-scheme photocatalysts, *Mater. Today* 47 (2021) 75–107, <https://doi.org/10.1016/j.mattod.2021.02.017>.
- [30] J. Zhao, M. Ji, H. Chen, Y. Weng, J. Zhong, Y. Li, S. Wang, Z. Chen, J. Xia, H. Li, Interfacial chemical bond modulated Bi<sub>19</sub>S<sub>27</sub>Br<sub>3</sub>/g-C<sub>3</sub>N<sub>4</sub> Z-scheme heterojunction for enhanced photocatalytic CO<sub>2</sub> conversion, *Appl. Catal. B: Environ.* 307 (2022), 121162, <https://doi.org/10.1016/j.apcatb.2022.121162>.

[31] J. Wang, W. Lin, S. Zhou, Z. Li, H. Hu, Y. Tao, S. Zhou, X. Zhao, Y. Kong, Probing the formation and optical properties of  $Ti^{3+}$ - $TiO_2$  with (001) exposed crystal facet by ethanol-assisted fluorination, *N. J. Chem.* 45 (2021) 12453–12463, <https://doi.org/10.1039/d1nj01591e>.

[32] I. Romero-Muniz, A. Mavrandonakis, P. Albacete, A. Vega, V. Brío, F. Zamora, A. E. Platero-Prats, Unveiling the local structure of palladium loaded into imine-linked layered covalent organic frameworks for cross-coupling catalysis, *Angew. Chem. Int. Ed.* 59 (2020) 13013–13020, <https://doi.org/10.1002/anie.202004197>.

[33] C. Kang, Z. Zhang, V. Wee, A.K. Usadi, D.C. Calabro, L.S. Baugh, S. Wang, Y. Wang, D. Zhao, Interlayer shifting in two-dimensional covalent organic frameworks, *J. Am. Chem. Soc.* 142 (2020) 12995–13002, <https://doi.org/10.1021/jacs.0c03691>.

[34] F. Xu, K. Meng, B. Cheng, S. Wang, J. Xu, J. Yu, Unique S-scheme heterojunctions in self-assembled  $TiO_2$ / $CspbBr_3$  hybrids for  $CO_2$  photoreduction, *Nat. Commun.* 11 (2020) 4613, <https://doi.org/10.1038/s41467-020-18350-7>.

[35] Q. Han, C. Wu, H. Jiao, R. Xu, Y. Wang, J. Xie, Q. Guo, J. Tang, Rational design of high-concentration  $Ti^{3+}$  in porous carbon-doped  $TiO_2$  nanosheets for efficient photocatalytic ammonia synthesis, *Adv. Mater.* 33 (2021), 2008180, <https://doi.org/10.1002/adma.202008180>.

[36] J. Wan, W. Chen, C. Jia, L. Zheng, J. Dong, X. Zheng, Y. Wang, W. Yan, C. Chen, Q. Peng, D. Wang, Y. Li, Defects effects on  $TiO_2$  nanosheets: stabilizing single atomic Site Au and promoting catalytic properties, *Adv. Mater.* 30 (2018), 1705369, <https://doi.org/10.1002/adma.201705369>.

[37] S. Liang, X. Xiao, L. Bai, B. Liu, M. Yuan, P. Ma, M. Pang, Z. Cheng, J. Lin, Conferring Ti-based MOFs with defects for enhanced sonodynamic cancer therapy, *Adv. Mater.* 33 (2021), 2100333, <https://doi.org/10.1002/adma.202100333>.

[38] Y. Han, Y.G. Wang, W. Chen, R. Xu, L. Zheng, J. Zhang, J. Luo, R.A. Shen, Y. Zhu, W.C. Cheong, C. Chen, Q. Peng, D. Wang, Y. Li, Hollow N-doped carbon spheres with isolated cobalt single atomic sites: superior electrocatalysts for oxygen reduction, *J. Am. Chem. Soc.* 139 (2017) 17269–17272, <https://doi.org/10.1021/jacs.7b10194>.

[39] H. Zhong, C. Yang, L. Fan, Z. Fu, X. Yang, X. Wang, R. Wang, Dyadic promotion of photocatalytic aerobic oxidation via the Mott-Schottky effect enabled by nitrogen-doped carbon from imidazolium-based ionic polymers, *Energy Environ. Sci.* 12 (2019) 418–426, <https://doi.org/10.1039/c8ee02727g>.

[40] C. Cheng, B. He, J. Fan, B. Cheng, S. Cao, J. Yu, An inorganic/organic S-scheme heterojunction  $H_2$  production photocatalyst and its charge transfer mechanism, *Adv. Mater.* 33 (2021), 2100317, <https://doi.org/10.1002/adma.202100317>.

[41] P. Xia, S. Cao, B. Zhu, M. Liu, M. Shi, J. Yu, Y. Zhang, Designing a 0D/2D S-scheme heterojunction over polymeric carbon nitride for visible-light photocatalytic inactivation of bacteria, *Angew. Chem. Int. Ed.* 59 (2020) 5218–5225, <https://doi.org/10.1002/anie.201916012>.

[42] Z. Wang, Z. Wang, X. Zhu, C. Ai, Y. Zeng, W. Shi, X. Zhang, H. Zhang, H. Si, J. Li, C. Wang, S. Lin, Photodepositing CdS on the active cyano groups decorated g-C<sub>3</sub>N<sub>4</sub> in Z-scheme manner promotes visible-light-driven hydrogen evolution, *Small* 17 (2021), 2102699, <https://doi.org/10.1002/smll.202102699>.

[43] C. Liu, D. Kong, P.C. Hsu, H. Yuan, H.W. Lee, Y. Liu, H. Wang, S. Wang, K. Yan, D. Lin, P.A. Maraccini, K.M. Parker, A.B. Boehm, Y. Cui, Rapid water disinfection using vertically aligned MoS<sub>2</sub> nanofilms and visible light, *Nat. Nanotechnol.* 11 (2016) 1098–1104, <https://doi.org/10.1038/nnano.2016.138>.

[44] M. Melchionna, P. Fornasiero, Updates on the roadmap for photocatalysis, *ACS Catal.* 10 (2020) 5493–5501, <https://doi.org/10.1021/acscatal.0c01204>.

[45] S. Cao, L. Piao, Considerations for a more accurate evaluation method for photocatalytic water splitting, *Angew. Chem., Int. Ed.* 59 (2020) 18312–18320, <https://doi.org/10.1002/anie.202009633>.

[46] I.M. Hill, S. Hanspal, Z.D. Young, R.J. Davis, DRIFTS of probe molecules adsorbed on magnesia, zirconia, and hydroxyapatite catalysts, *J. Phys. Chem. C* 119 (2015) 9186–9197, <https://doi.org/10.1021/jp509889j>.

[47] T. Kong, Y. Jiang, Y. Xiong, Photocatalytic  $CO_2$  conversion: What can we learn from conventional  $CO_2$  hydrogenation? *Chem. Soc. Rev.* 49 (2020) 6579–6591, <https://doi.org/10.1039/c9cs00920e>.

[48] J. Sheng, Y. He, J. Li, C. Yuan, H. Huang, S. Wang, Y. Sun, Z. Wang, F. Dong, Identification of halogen-associated active sites on bismuth-based perovskite quantum dots for efficient and selective  $CO_2$ -to-CO photoreduction, *ACS Nano* 14 (2020) 13103–13114, <https://doi.org/10.1021/acsnano.0c04659>.

[49] H.J. Freund, M.W. Roberts, Surface chemistry of carbon dioxide, *Surf. Sci. Rep.* 25 (1996) 225–273, [https://doi.org/10.1016/s0167-5729\(96\)00007-6](https://doi.org/10.1016/s0167-5729(96)00007-6).

[50] D. Mao, S. Yang, Y. Hu, H. He, S. Yang, S. Zheng, C. Sun, Z. Jiang, X. Qu, P. K. Wong, Efficient  $CO_2$  photoreduction triggered by oxygen vacancies in ultrafine Bi<sub>5</sub>O<sub>3</sub>Br nanowires, *Appl. Catal. B: Environ.* 321 (2023), 122031, <https://doi.org/10.1016/j.apcatb.2022.122031>.

[51] X. Chang, T. Wang, J. Gong, CO<sub>2</sub> photo-reduction: insights into CO<sub>2</sub> activation and reaction on surfaces of photocatalysts, *Energy Environ. Sci.* 9 (2016) 2177–2196, <https://doi.org/10.1039/c6ee00383d>.

[52] N. Li, B. Wang, Y. Si, F. Xue, J. Zhou, Y. Lu, M. Liu, Toward high-value hydrocarbon generation by photocatalytic reduction of CO<sub>2</sub> in water vapor, *ACS Catal.* 9 (2019) 5590–5602, <https://doi.org/10.1021/acscatal.9b00223>.

[53] S. Yang, H. Li, H. Li, W. Qi, Q. Zhang, J. Zhu, P. Zhao, L. Chen, Rational design of 3D carbon nitrides assemblies with tunable nano-building blocks for efficient visible-light photocatalytic  $CO_2$  conversion, *Appl. Catal. B: Environ.* 316 (2022), 121612, <https://doi.org/10.1016/j.apcatb.2022.121612>.